ADVANCES IN ATMOSPHERIC SCIENCES, VOL. 29, NO. 1, 2012, 10–28

Characteristics and Nonlinear Growth of the Singular Vector Related to a Heavy Rainfall Case over the Korean Peninsula

Yonghan CHOI, Joowan KIM, and Dong-Kyou LEE*

School of Earth and Environmental Sciences, Seoul National University, Seoul 151-742, *South Korea*

(Received 1 November 2010; revised 3 June 2011)

ABSTRACT

In this study, singular vectors related to a heavy rainfall case over the Korean Peninsula were calculated using the fifth-generation Pennsylvania State University–National Center for Atmospheric Research Mesoscale Model (MM5) adjoint modeling system. Tangent linear and adjoint models include moist physical processes, and a moist basic state and a moist total energy norm were used for the singular-vector calculations. The characteristics and nonlinear growth of the first singular vector were analyzed, focusing on the relationship between the basic state and the singular vector.

The horizontal distribution of the initial singular vector was closely related to the baroclinicity index and the moisture availability of the basic state. The temperature-component energy at a lower level was dominant at the initial time, and the kinetic energy at upper levels became dominant at the final time in the energy profile of the singular vector.

The nonlinear growth of the singular vector appropriately reflects the temporal variations in the basic state. The moisture-component energy at lower levels was dominant at earlier times, indicating continuous moisture transport in the basic state. There were a large amount of precipitation and corresponding latent heat release after that period because the continuous moisture transport created favorable conditions for both convective and nonconvective precipitation. The vertical propagation of the singular-vector energy was caused by precipitation and the corresponding latent heating in the basic state.

Key words: singular vector, nonlinear growth, heavy rainfall, MM5 adjoint modeling system

Citation: Choi, Y., J. Kim, and D.-K. Lee, 2012: Characteristics and nonlinear growth of the singular vector related to a heavy rainfall case over the Korean Peninsula. *Adv. Atmos. Sci.*, **29**(1), 10–28, doi: 10.1007/s00376-011-0194-5.

1. Introduction

Singular vectors are optimal perturbations that grow most rapidly in terms of a norm for a given basic state and optimization time interval (Kim and Morgan, 2002). Singular vectors have been widely used for both theoretical and practical purposes since they were introduced to atmospheric science. For example, singular vectors have been used for studies on the predictability of numerical weather prediction models (Lorenz, 1965; Farrell, 1990; Buizza and Palmer, 1995; Ehrendorfer and Errico, 1995; Palmer, 1996; Errico et al., 2001), the design of initial perturbations for ensemble forecasting (Buizza et al., 1993; Molteni et al., 1996; Ehrendorfer and Tribbia, 1997; Gelaro et al., 1998; Hamill et al., 2000), and target (or adaptive) observations (Buizza and Montani, 1999; Gelaro et al., 1999; Majumdar et al., 2002; Majumdar et al., 2006; Wu et al., 2009; Yamaguchi et al., 2009).

Hoskins et al. (2000) calculated singular vectors using the European Center for Medium-Range Weather Forecasts Ensemble Prediction System (ECMWF EPS) to investigate the influence of the basic state on the structure of the singular vectors. They found that amplification factor, geographical distribution, vertical energy profile, and energy spectrum are sensitive to the basic state. Coutinho et al. (2004) studied the impact of moist, linearized physical parameterization on extratropical singular vectors using the ECMWF Integrated Forecasting System (IFS). The inclusion

---

*Corresponding author: Dong-Kyou LEE, dklee@snu.ac.kr of moist linear physics resulted in a shift to smaller horizontal scales and enhanced growth for the singular vectors, and large-scale condensation was found to be more important than cumulus convection. Hoskins and Coutinho (2005) computed singular vectors using the full-physics ECMWF global model and a dry total energy norm for high-impact European cyclones. Large-scale latent heat release is crucial to obtaining the relevant singular vectors, and this is consistent with the results of Coutinho et al. (2004).

Few studies on singular vectors have used regional models and the corresponding tangent linear/adjoint models compared to global models. Ehrendorfer and Errico (1995) computed singular vectors by using the National Center for Atmospheric Research Mesoscale Adjoint Modeling System version 1 (NCAR MAMS1) developed by Errico et al. (1994). Dry total energy norm and dry tangent linear/adjoint models were used. Singular-vector calculations were performed for two different synoptic cases: explosive cyclogenesis over the North Atlantic and Alpine lee cyclogenesis. They analyzed the eigenvalues spectra, horizontal structures, and vertical energy profiles of the singular vectors, and they also mentioned the mesoscale predictability based on the eigenvalues spectra. Ehrendorfer et al. (1999) used the moist version of MAMS2 and a moist total energy norm to calculate singular vectors related to winter and summer cases. They found that the consideration of moisture leads to faster growth of perturbations and the appearance of newly growing structures. The growth rates of the singular vectors were more sensitive to the choice of the basic state and the tangent linear model (dry or moist) than to the choice of the norm (dry or moist total energy). The spectra of singular values were computed (Errico et al., 2001), and singular vectors with norms based on the inverse of variances in the initial-condition uncertainty and precipitation rate were calculated (Errico et al., 2004) using MAMS2.

Recently, the fifth-generation Pennsylvania State University-NCAR Mesoscale Model (MM5) and its adjoint modeling system (Zou et al., 1998) were used to calculate singular vectors for a tropical cyclone (TC). Kim and Jung (2009a) used the MM5 adjoint modeling system and a dry total-energy norm (including vertical wind perturbations) to compute singular vectors for TC Usagi (2007). They found that, relatively far from the region of TC recurvature, singular vectors near the TC center were important and that closer to the TC recurvature, singular vectors in the mid-latitude trough region were important for adaptive observation strategies. Kim and Jung (2009b) investigated the effects of moist linear physics (large-scale precipitation) and a moist total-energy norm on the structures and growth rates of singular vectors using the MM5 adjoint modeling system. They found that, given large-scale precipitation as the linear moist physics, the singular-vector horizontal structure (smaller scale), vertical energy profile (closer to the lower boundary), and growth rate (greater growth rate) with the moist total energy norm show the largest difference compared to those using other norms.

On the basis of the results reported by Badger and Hoskins (2001), Hoskins et al. (2000) suggested growth mechanisms for the singular vector calculated using the ECMWF EPS. Shorter optimization time interval (OTI) singular vectors grow by unshielding vertically compact potential vorticity (PV) structures and untilting westward-tilted troughs as they propagate upward. Longer OTI singular vectors also grow by unshielding and untilting their structures initially. The interaction between the interior PV of the singular vector and the temperature perturbation at the surface enables longer-term normal-mode-like (i.e., exponential) growth after the initial growth. This normal-mode-like growth can only be observed for the longer OTI singular vectors because their initial locations are lower than those of the shorter OTI singular vectors in the troposphere. Reynolds et al. (2001) examined the relationships between singular vectors and the transient features in the background flow by analyzing potential vorticity and $\boldsymbol{Q}$-vector. Montani and Thorpe (2002) indicated that part of the singular vector below 500 hPa is responsible for the singular-vector energy growth.

In this study, singular vectors were calculated using a complicated regional adjoint modeling system, that is, the MM5 adjoint modeling system like in Kim and Jung (2009a, b). However, the modeling system in this study was not used for extratropical or TC cases like those in previous studies but rather for a heavy rainfall case over the Korean Peninsula. Moist linear physics schemes, including a convective scheme as well as a large-scale precipitation scheme, and moist total energy norm were used to calculate singular vectors related to a heavy rainfall case in this study. To our knowledge, singular vectors for heavy rainfall have not yet been studied. Hoskins et al. (2000) suggested growth mechanisms for the singular vector calculated from the ECMWF global model using dry linear physics and the dry total energy norm. In this study, nonlinear growth of the singular vector calculated from the MM5 adjoint modeling system was investigated using moist linear physics and moist total energy norm.

The purposes of this study were to analyze the characteristics of the first singular vector and the relationships between the singular vector and the basic state, and to elucidate the mechanism underlying the nonlinear growth of the singular vector, especially the vertical propagation of singular-vector energy. In section 2, theoretical backgrounds of singular vectors are summarized, and brief descriptions of a numerical experiment and a heavy rainfall case are given in section 3. The characteristics and nonlinear growth of the singular vector are discussed in section 4. The conclusion is presented in section 5.

2. Theoretical background

Singular vectors are those structures that grow most rapidly in terms of a specified norm during an optimization time interval in a linear sense. The theoretical background of singular vectors is briefly explained in this section. A full description of the theoretical background of singular vectors can be found in previous literature (e.g., Ehrendorfer and Errico, 1995; Ehrendorfer et al., 1999; Errico et al., 2004; Kalnay, 2004; Kim and Jung, 2009a; Kim and Jung, 2009b).

In this study, a moist total energy norm (Ehrendorfer et al., 1999; Errico et al., 2004) that excludes the contribution from a surface pressure term was used both at initial and final times:

$$E = \frac{1}{N_\mathrm{w}} \sum_{i,j,k} \Delta\sigma_k (u'^2_{i,j,k} + v'^2_{i,j,k}) + \frac{1}{N_\mathrm{t}} \frac{c_p}{T_\mathrm{r}} \times \sum_{i,j,k} \Delta\sigma_k T'^2_{i,j,k} + \frac{1}{N_\mathrm{t}} \frac{L^2}{c_p T_\mathrm{r}} \sum_{i,j,k} \Delta\sigma_k q'^2_{i,j,k} \quad (1)$$

where E is moist total energy, u and v are zonal and meridional components of wind respectively, T is temperature, q is the water vapor mixing ratio, and a prime denotes the perturbation quantity. $N_\mathrm{w} = (n_x - 2)(n_y - 2)$ is the number of grid points for the wind field and $N_\mathrm{t} = (n_x - 3)(n_y - 3)$ is the number of grid points for the thermodynamic field. Indices, i, j, and k represent zonal, meridional, and vertical directions, respectively, and $\Delta\sigma_k$ denotes the interval between adjacent levels. In this equation, c_p is the specific heat of dry air at constant pressure, T_r is the reference temperature, and L is the latent heat of condensation per unit mass with numerical values of 1005.7 J kg^{-1} K^{-1}, 270 K, and 2.5104×10^6 J kg^{-1}, respectively.

Singular vectors were calculated from the maximization problem as follows. The initial (t=0) amplitude of the perturbation (of the state vector) in terms of the norm was constrained to be unity, and the amplitude of the perturbation at the optimization time ($t = \tau_\mathrm{opt}$) in terms of the norm was maximized:

$$\frac{<\boldsymbol{APx}_t, \boldsymbol{APx}_t>}{<\boldsymbol{APx}_0, \boldsymbol{APx}_0>} = \frac{<\boldsymbol{APLx}_0, \boldsymbol{APLx}_0>}{<\boldsymbol{APx}_0, \boldsymbol{APx}_0>} = \frac{<\boldsymbol{APLQy}_0, \boldsymbol{APLQy}_0>}{<\boldsymbol{APQy}_0, \boldsymbol{APQy}_0>}, \quad (2)$$

where the inner product is denoted by $<,>$, matrix $\boldsymbol{A}$ defines the specified norm, matrix $\boldsymbol{P}$ (projection matrix) picks up some variables required to calculate the norm from the entire variables of the state vector, matrix $\boldsymbol{Q}$ (retrieval matrix) operates oppositely to matrix $\boldsymbol{P}$, and $\boldsymbol{L}$ is a tangent linear model operator. In this equation, $\boldsymbol{x}_0$ is the perturbation of the state vector at t=0, $\boldsymbol{x}_t$ is the perturbation of the state vector at t $=\tau_\mathrm{opt}$, and $\boldsymbol{y}_0=\boldsymbol{Q}^{-1}\boldsymbol{x}_0$. Matrix $\boldsymbol{B}$ was introduced to reduce the generalized eigenvalue problem related to Eq. (2) to an ordinary eigenvalue problem:

$$\frac{<\boldsymbol{APLQB}^{-1}\boldsymbol{z}_0, \boldsymbol{APLQB}^{-1}\boldsymbol{z}_0>}{<\boldsymbol{z}_0, \boldsymbol{z}_0>} = \frac{\boldsymbol{z}_0^\mathrm{T}(\boldsymbol{B}^{-1})^\mathrm{T}\boldsymbol{Q}^\mathrm{T}\boldsymbol{L}^\mathrm{T}\boldsymbol{P}^\mathrm{T}\boldsymbol{A}^\mathrm{T}\boldsymbol{APLQB}^{-1}\boldsymbol{z}_0}{\boldsymbol{z}_0^\mathrm{T}\boldsymbol{z}_0}, \quad (3)$$

where $\boldsymbol{B} = \boldsymbol{APQ}$ and $\boldsymbol{z}_0 = \boldsymbol{By}_0$.

It can be easily shown that this maximization problem is equivalent to the ordinary eigenvalue problem by introducing a Lagrangian and setting its derivatives equal to zero:

$$(\boldsymbol{B}^{-1})^\mathrm{T}\boldsymbol{Q}^\mathrm{T}\boldsymbol{L}^\mathrm{T}\boldsymbol{P}^\mathrm{T}\boldsymbol{A}^\mathrm{T}\boldsymbol{APLQB}^{-1}\boldsymbol{z}_0 = \lambda\boldsymbol{z}_0 , \quad \text{with} \quad \boldsymbol{z}_0^\mathrm{T}\boldsymbol{z}_0 = 1 . \quad (4)$$

Finally, singular vectors were calculated from the eigenvectors, $\boldsymbol{z}_0$ and singular values were calculated from the eigenvalues, λ.

3. Numerical model, experiment design, and a heavy rainfall case

3.1 *Numerical model and experiment design*

The MM5 adjoint modeling system[a] was used to calculate singular vectors in this study. The adjoint modeling system consists of a nonlinear model, a tangent linear model, and an adjoint model. The nonlinear model is based on the MM5 version 1 (Grell et al., 1993).

---

[a] Vukicevic and Errico (1993) noted the problems related to nonphysical oscillations in tangent linear and adjoint models of the MM4, the previous version of the MM5. However, these problems can be removed by using the method proposed by Zou et al. (2001), and the problems affect only the adjoint sensitivity results, not the singular vector results.

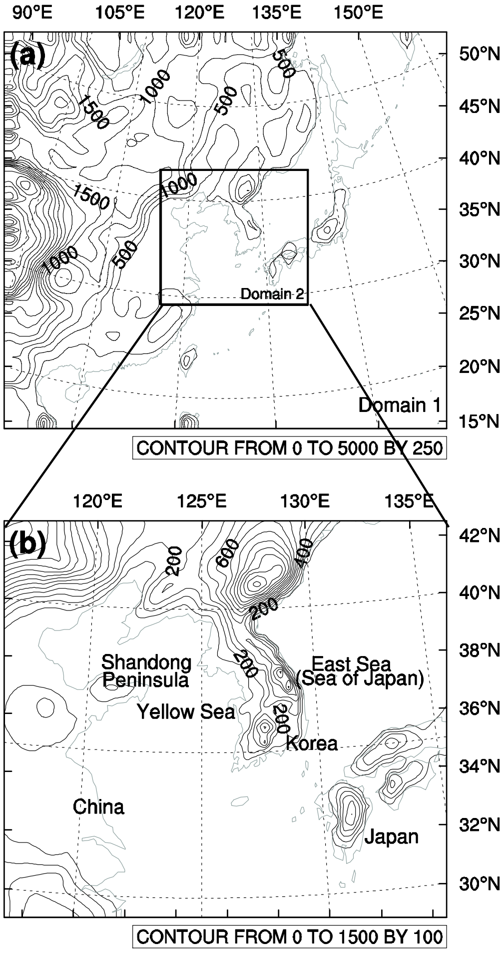

Fig. 1. Geographical area and terrain height (contour interval of 250 or 100 m) for (a) domain 1 and (b) domain 2. Singular-vector calculation was performed on domain 2.

Basic state (or nonlinear model trajectory) is a reference state for the integration of the tangent linear and adjoint models, and it was considered equivalent to the integration of the nonlinear model in this study. One-way nested domains (domain 1 and 2) were used for the integration of the nonlinear model (Fig. 1). The number of grid points for both domain 1 and 2 was 58 × 52, and the horizontal grid spacing of domains 1 and 2 were 90 km and 30 km, respectively. The number of half-sigma levels for all the domains[b] was 10, from 0.05 to 0.95, with an identical interval of 0.1, and the model top was 50 hPa. The National Centers for Environmental Prediction/National Center for Atmospheric Research (NCEP/NCAR) reanalysis data with a horizontal resolution of T62 (~209 km) were used for the initial and boundary conditions of domain 1.

Physical parameterization schemes used for the integration of the nonlinear model included the Anthes-Kuo cumulus parameterization scheme (Kuo, 1974), a bulk aerodynamic formulation of planetary boundary layer, stable precipitation (i.e., large-scale precipitation), a simple cooling radiation scheme, horizontal diffusion, vertical diffusion, and dry convective adjustment. The stable precipitation was simply parameterized by precipitating any moisture in excess of 100% relative humidity and ignoring any subsequent evaporation.

Singular-vector calculation was performed in domain 2, and physical parameterization schemes used for the tangent linear and adjoint models integration were the same as those for the nonlinear model. The initial time for domain 2 integration (i.e., singular vector calculation) was 1200 UTC on 29 June 1994, and the optimization time interval was 24 h from 1200 UTC on 29 June to 1200 UTC on 30 June 1994. The moist total energy norm introduced in section 2 was used for the singular-vector calculation.

The eigenproblem related to the singular vector calculation [Eq. (4)] could not be solved directly because the dimension of eigenproblems is very large, and it is impossible to know explicitly every element of the matrix associated with the eigenproblem. The F12FBF FORTRAN library routine (NAG, 2005) developed at the Numerical Algorithm Group (NAG) was used to compute singular vectors iteratively. This routine was equivalent to the Lanczos algorithm for symmetric problems (Strang, 1986).

3.2 *A heavy rainfall case*

In the heavy rainfall case studied here, a surface low moving from the Shandong Peninsula to the Korean Peninsula induced a large amount of precipitation over the Korean Peninsula. The amount of 24-h accumulated precipitation, from 1200 UTC 29 June 1994 to 1200 UTC 30 June 1994, was >200 mm over the central part of South Korea. The maximum accumulated precipitation amount in 24 h was 244 mm at Yeongju, and the 1-h accumulated precipitation at Yeongju was 60 mm at 1000 UTC 30 June 1994 (Fig. 2a). The precipitation distribution and precipitation amount simulated in the nonlinear model integration were similar to the observations (Fig. 2b).

Synoptic analyses made using the European Center for Medium-Range Weather Forecasts 40-year reanalysis (ECMWF ERA-40) data for 1200 UTC 29 June 1994 are shown in Figs. 2c and d. At 1200 UTC 29 June 1994, there was strong upper-level divergence related to the upper-level jet stream, and this

---

[b] The number of vertical levels used in this study was restricted to 10 because of the enormous computational cost and memory requirements.

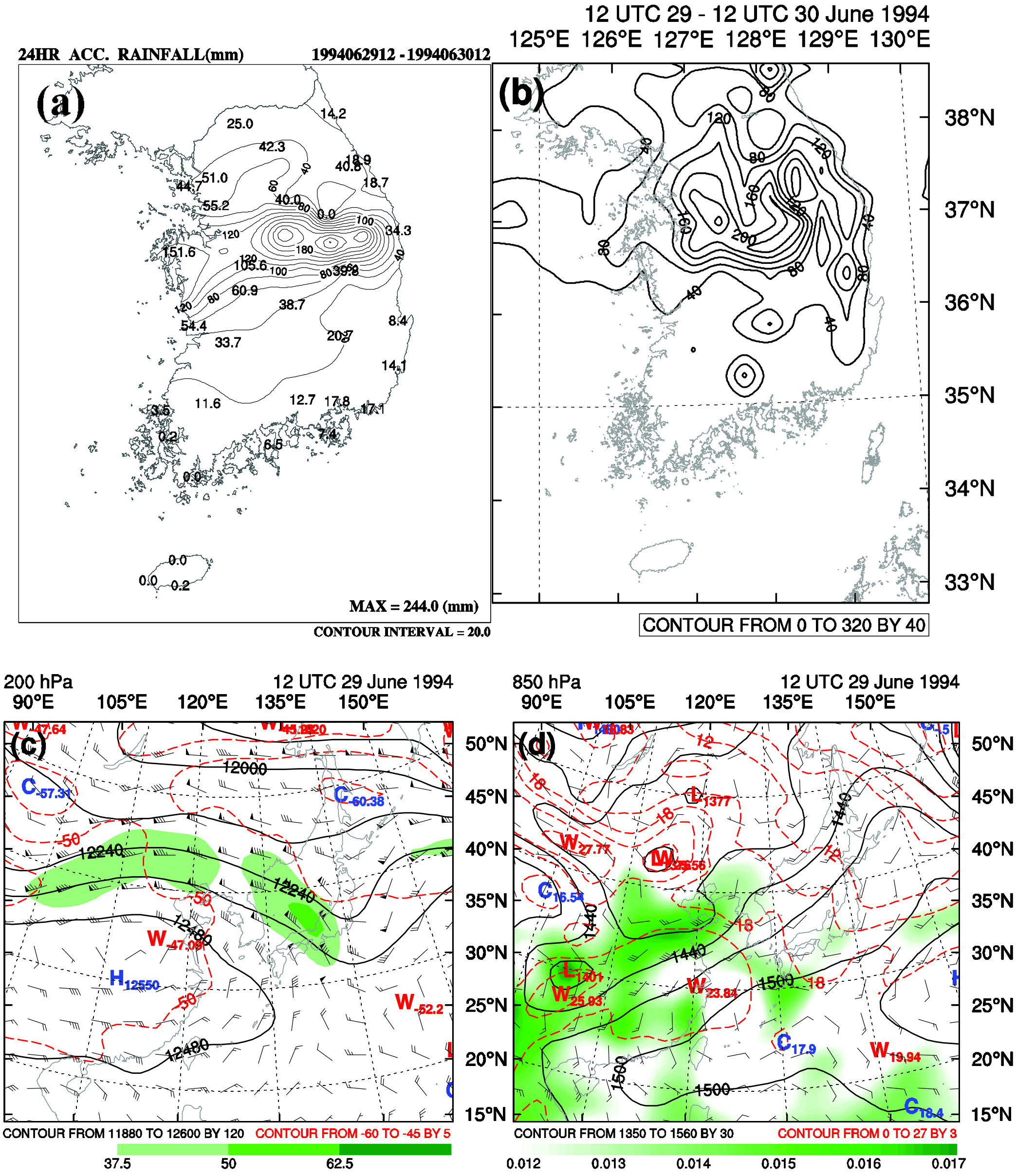

Fig. 2. The 24-h accumulated precipitation distribution over South Korea (top panel, mm, from 1200 UTC 29 June to 1200 UTC 30 June 1994) for (a) surface observations and (b) nonlinear model simulation. Synoptic analyses at 1200 UTC 29 June 1994 (bottom panel). (c) geopotential height (black solid, contour interval of 120 m), temperature (red dashed, contour interval of 5 K), wind speed (shaded, >37.5 m s^{-1}), and wind vector at 200 hPa and (d) geopotential height (black solid, contour interval of 30 m), temperature (red dashed, contour interval of 3 K), water-vapor mixing ratio (shaded, >0.012 kg kg^{-1}), and wind vector at 850 hPa.

upper-level large-scale forcing induced upward motion. At 200 hPa level, cold and dry air from the northern parts of China was advected to the Korean Peninsula by a northerly or northwesterly flow (Fig. 2c). The lower-level trough at 850 hPa level was west of the surface low. This westward-tilted structure implies that the upstream regions of the Korean Peninsula were baroclinically unstable. Warm and moist air from the central and southern parts of China was advected at 850 hPa level by a southwesterly flow with a speed of nearly 20 m s^{-1} (Fig. 2d).

At 0000 UTC 30 June, the surface low deepened as it moved downstream. Warm and moist air was transported to the Korean Peninsula continuously at 850 hPa by the southwesterly flow between cyclonic circulation and anticyclonic circulation over the Yellow

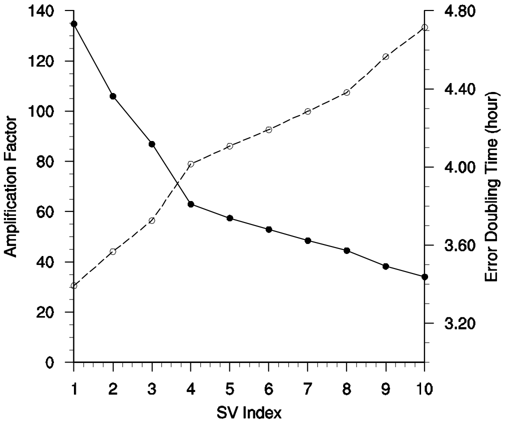

Fig. 3. Amplification factor (solid line with filled circles) and error doubling time (h, dashed line with open circles) for the first 10 SVs.

Sea (not shown).

The heavy rainfall case examined in this study was characterized by the advection of warm and moist air at lower levels and the advection of cold and dry air at upper levels. This synoptic environment provided favorable conditions for the development of the precipitating system. In other words, convective (conditional) instability as well as baroclinic instability caused torrential rainfall over the Korean Peninsula. Note that this synoptic pattern has been frequently observed in the heavy rainfall cases over the Korean Peninsula (Lee et al., 2008). Synoptic environments related to the heavy rainfall were well simulated in the nonlinear model run (not shown).

4. Results and discussion

4.1 *Characteristics of the singular vectors*

Figure 3 shows an amplification factor (or singular value) and its corresponding error-doubling time as a function of the singular-vector index. The amplification factor was calculated from the ratio of the norms at the initial and final times, and the error-doubling time is given as $t_{\rm d} \equiv \tau_{\rm opt}\ln 2/\ln\lambda$, assuming exponential growth. By definition, the amplification factor decreases and the error-doubling time increases with the increasing singular-vector index. The amplification factor of the first singular vector was $\sim$135, and the corresponding error-doubling time was $\sim$3.39 h. The amplification factors (error-doubling times) of the second, third, and fourth singular vectors were $\sim$106 (3.57 h), 87 (3.73 h), and 63 (4.02 h), respectively. The decreasing rate of the amplification factor from the first to the fourth singular vector ($\sim$72) was greater than that from the fifth to the tenth singular vector ($\sim$19). The characteristics and nonlinear growth of the first singular vector (hereafter denoted as SV1) are analyzed below, although a total of 10 singular vectors were computed in this study.

The horizontal distributions of an initial SV1 and a final SV1 are shown in Fig. 4. Each component of the SV1 was plotted at its maximum-amplitude level. A level was determined as a maximum-amplitude level when the absolute value of each component of the SV1 was the greatest at that level. The initial SV1 was located near the Shandong Peninsula, the location of surface low at the initial time. The amplitude for the temperature component of the initial SV1 was the greatest and that for the moisture component was the smallest. The temperature and moisture components were more localized than the zonal wind and meridional wind components. The meridional wind, temperature, and moisture components were in phase, but the zonal wind component was out of phase with the other components when all of the components were compared at the same level (e.g., at the 0.85-sigma level; figures not shown). Positive values of the temperature component were collocated with positive values of the meridional wind component, and negative values of the temperature component were collocated with negative values of the meridional wind component, implying a decrease of horizontal temperature gradient or an energy conversion of baroclinic waves. The final SV1 was located over the East Sea (Sea of Japan), downstream of the location of the initial SV1. The location of the final SV1 was related to the distribution of 24-h accumulated precipitation (Fig. 2b). The amplitudes of the zonal wind and meridional wind components were greater than those of the temperature and moisture components. In addition, the horizontal extents for all the components of the final SV1 increased compared to those of the initial SV1[c].

Analyzing the energy characteristics of the SV1 was important because the (moist) total energy norm was used in this study. Figure 5 shows the vertical profile of the SV1 total energy, kinetic energy (contributions from the zonal wind and meridional wind components), temperature-component energy, and moisture-component energy at the initial and final times. The total energy of the initial SV1 had an amplitude of one, and that of the final SV1 was normalized by its singular value. The temperature-component energy was dominant, and it was concentrated at a lower level, the 0.85-sigma level ($\sim$857 hPa) at the initial time. There

---

[c] Contour or shading interval should be same when horizontal extent is considered. When the contour or shading interval is set to the same value, the above statements on the horizontal extent are still valid (figures not shown), and they are consistent with Fig. 6.

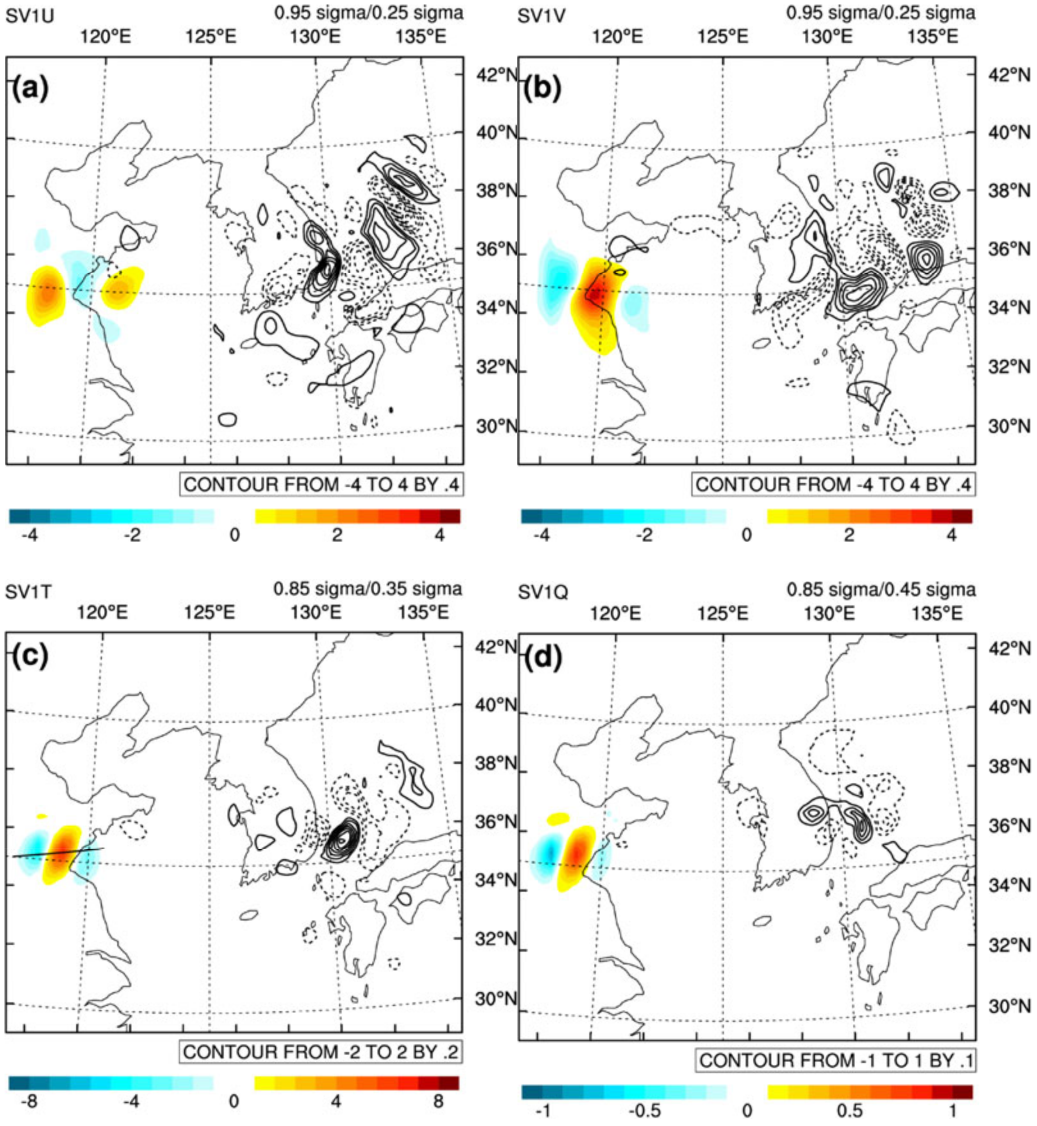

Fig. 4. Horizontal distribution of initial SV1 (shaded) and final SV1 (contour, negative values are denoted by dashed contours, normalized by its singular value). (a) zonal wind component (m s^{-1}), (b) meridional wind component (m s^{-1}), (c) temperature component (K), and (d) moisture component (g kg^{-1}). Each plot was made at its maximum level and the level was indicated at upper-right corner (initial/final).

were two peaks in the energy profile at the final time. One peak was located at an upper level, the 0.25-sigma level (∼287 hPa), related to the kinetic energy. The other peak was located at a relatively lower level, the 0.75-sigma level (∼762 hPa), related to the moisture-component energy. The initial SV energy related to the temperature component at a lower level was converted to the final SV energy related to the wind components at an upper level, a result that is consistent with previous studies (Ehrendorfer et al., 1999; Coutinho et al., 2004) for extratropical cyclones. The mechanism associated with the vertical propagation of the SV energy is explained in the next subsection.

The spectral distributions of the total energy, kinetic energy, and temperature- and moisture-components energy for the initial and final SV1 are shown in Fig. 6. The energy spectra were calculated using the Discrete Cosine Transform (DCT, Denis et al., 2002) to avoid the aliasing effect of aperiodicity. A spectral peak appeared near the wavelength of 167 km (meso-β) at the initial time. The peak moved toward the longer wavelength (∼214 km, meso-α) at the final time. The total energy with wavelength >214 km and <115 km increased, and that between 214 km and

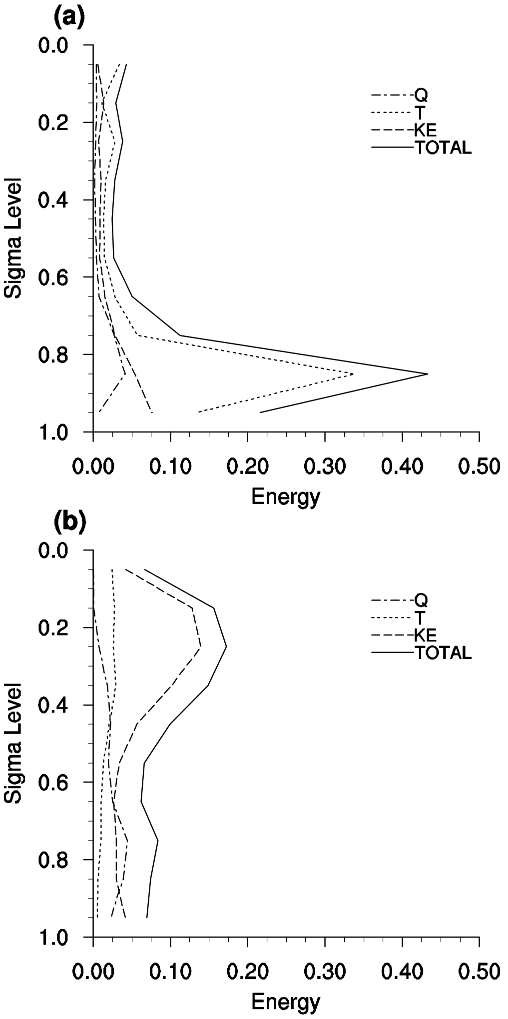

Fig. 5. Vertical profile of SV1 total energy (J kg^{-1}, solid line), kinetic energy (J kg^{-1}, dashed line), temperature-component energy (J kg^{-1}, dotted line), and moisture-component energy (J kg^{-1}, dash-dotted line). (a) initial time and (b) final time. Final SV1 was normalized by its singular value to make its total energy equal to one.

115 km decreased (Fig. 6a). The initial spectral peak of the total energy was related to a spectral peak of the temperature-component energy at the initial time. The intermediate-scale temperature-component energy decreased significantly, and the large-scale energy increased slightly (Fig. 6c). The final spectral peak of the total energy was related to a spectral peak of the kinetic energy at the final time. The kinetic energy over all of the scales increased, especially in the large-scale region (Fig. 6b). The moisture-component energy over nearly all the scales also increased, although the absolute value was smaller than the kinetic energy (Fig. 6d). Consequently, the intermediate-scale (mainly meso-β scale) temperature-component energy at the initial time was converted to the large-scale kinetic energy (greater than the meso-α scale) and the small-scale kinetic energy, mostly large-scale, at the final time by (linear) model dynamics and physics. Coutinho et al. (2004) showed the upscale energy transfer of the SV energy, energy transfer from a higher wavenumber region (i.e., small-scale region) to a lower wavenumber region (i.e., large-scale region), using the ECMWF global model. Although the upscale energy transfer indicated in Coutinho et al. (2004) was not shown clearly, the large-scale SV energy increased, whereas the intermediate-scale SV energy decreased in this study.

In summary, the initial SV1 coincided with the surface low (near the Shandong Peninsula) causing heavy rainfall over the Korean Peninsula. The initial temperature-component energy at lower levels was converted to the final kinetic energy at upper levels. Moreover, the initial spectral energy peak shifted toward the longer wavelength during the optimization time interval (24 h in this study).

4.2 *Nonlinear growth of the first singular vector*

Nonlinear growth of the SV1 was calculated as follows. CONTROL was defined as the nonlinear integration of an unperturbed initial condition, and it was considered equivalent to the basic state for tangent linear and adjoint model integrations. PERTURBED was defined as the nonlinear integration of a perturbed initial condition. The initial SV1 was re-scaled to be consistent with estimates of analysis uncertainty, and it was added to the unperturbed initial condition to create the perturbed initial condition. The nonlinear growth of the SV1 was computed from the difference between CONTROL and PERTURBED.

The temperature-component energy was dominant, and it was concentrated at lower levels in the SV energy profile at 1200 UTC on 29 June 1994 (Fig. 5a). To demonstrate the relationship between the peak of the temperature-component energy at lower levels and the basic state, the horizontal distributions for the temperature component of the initial SV1, baroclinicity index, and moisture availability at the initial time are given in Fig. 7a. The baroclinicity index was calculated as in Hoskins and Valdes (1990):

$$\sigma_{\mathrm{BI}} = 0.31 f \left| \frac{\partial \boldsymbol{V}}{\partial z} \right| N^{-1} , \tag{5}$$

where σ_{BI} is baroclinicity index, f is Coriolis parameter, $\boldsymbol{V}$ is horizontal wind vector, and N is Brunt-Väisälä frequency.

In the study of Coutinho et al. (2004), horizontal distributions of SVs were closely related to those of the baroclinicity index and moisture availability.

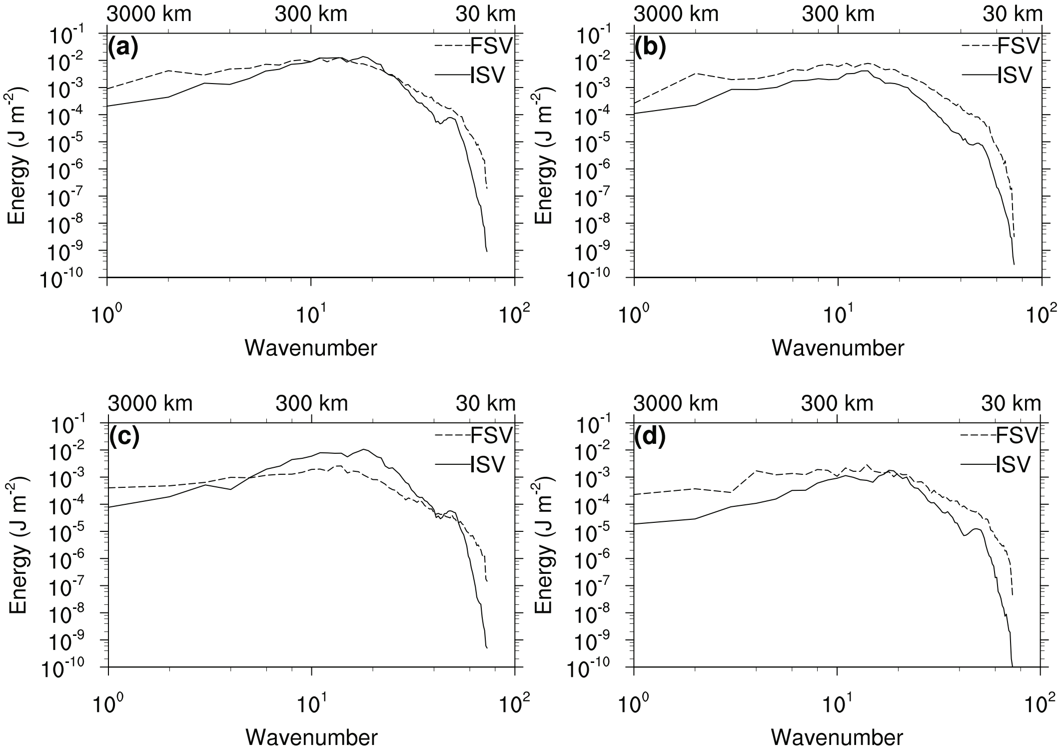

Fig. 6. Spectral distribution of (a) total energy, (b) kinetic energy, (c) temperature-component energy, and (d) moisture-component energy for initial SV1 (J m^{-2}, solid line) and final SV1 (J m^{-2}, dashed line) as a function of wavenumber.

The SV was located over regions of high baroclinicity, but its exact location did not coincide with the local maximum of the baroclinicity index. Instead, the SV shifted to the local maximum of the water-vapor mixing ratio. In this study, the maximum of the baroclinicity index occurred over the Yellow Sea, and that of the water-vapor mixing ratio was located near the Shandong Peninsula. As a result, the initial SV1 was not located over the Yellow Sea but was displaced toward the Shandong Peninsula. This result is consistent with the results of Coutinho et al. (2004), and implies the importance of moisture availability as well as baroclinic instability.

Vertical cross sections for the temperature component of the initial SV1 and the basic-state temperature at 1200 UTC on 29 June 1994 are shown in Fig. 7b. From the 0.95-sigma level (~952 hPa) to the 0.55-sigma level (~572 hPa), the temperature component of the initial SV1 tilted westward. This implies that the vertical structure of the initial SV1 was closely associated with the lower-level baroclinicity of the basic state mentioned in section 3.2. As the precipitating system developed, the baroclinicity gradually decreased and the upshear-tilted structure of the SV1 disappeared. After the initial time, the baroclinicity of the basic state remained same or decreased slightly; on the other hand, a large amount of moisture was transported vigorously in the basic state. Consequently, the peak of the temperature-component energy vanished shortly, and the peak of the moisture-component energy appeared afterward.

Vertical distributions of the SV1 energy from 1300 UTC to 1600 UTC 29 June 1994 are shown in Fig. 8. The initial temperature-component energy at lower levels became small, and the moisture-component energy at lower levels, the 0.75- and 0.85-sigma levels, became dominant within 1 h (Fig. 8a). At 1400 UTC 29 June, the moisture-component energy at the lower levels reached its peak amplitude (Fig. 8b). Subsequently, the moisture-component energy decreased gradually (Figs. 8c and d) until the kinetic energy at upper levels became dominant at 1800 UTC on 29 June (Fig. 11a). This 4-h dominance (from 1300 UTC to 1700 UTC 29 June) of the moisture-component energy at the lower levels also reflects the importance of moisture availability in this study.

Figure 9 shows the horizontal distributions of the moisture component of the SV1 and moisture flux vector computed from wind and moisture fields of the basic state from 1300 UTC to 1600 UTC 29 June 1994. The moisture component of the SV1 moved downstream continuously. From 1300 UTC to 1600 UTC

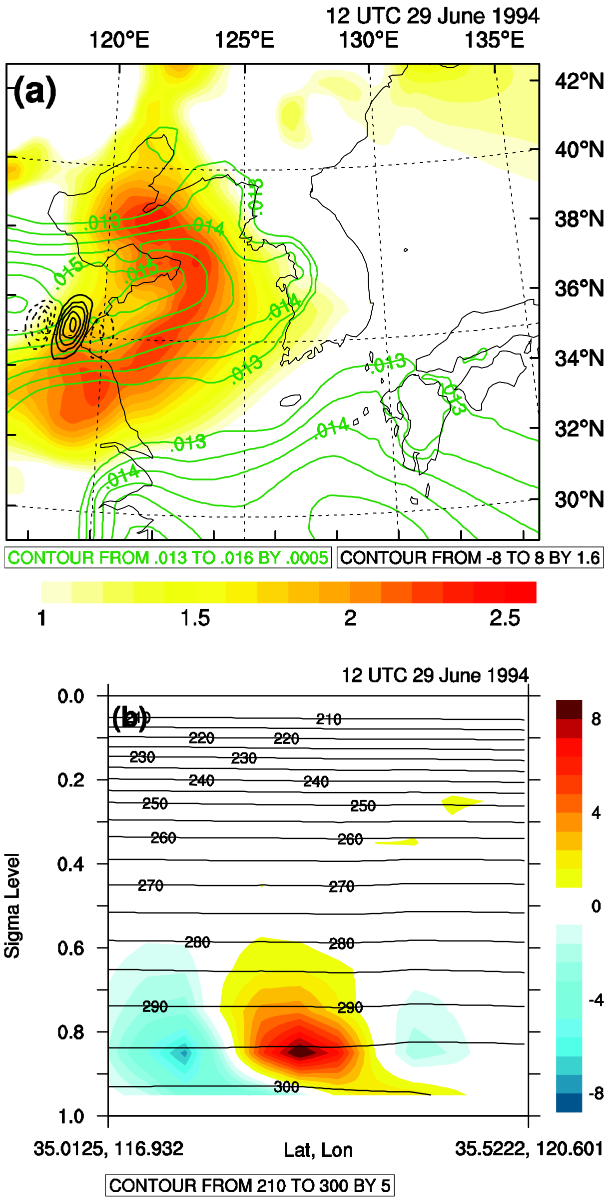

Fig. 7. (a) Temperature component of initial SV1 (K, black solid, negative values are denoted by dashed contours) at the 0.85-sigma level, lower-level baroclinicity index (shaded, $>1.0\times10^{-5}$ s^{-1}), and water-vapor mixing ratio (green solid, >0.013 kg kg^{-1}) at 1200 UTC 29 June 1994. (b) Vertical cross section along the line in Fig. 4c for temperature component of initial SV1 (shaded, K) and temperature of basic state (contour interval of 5 K) at 1200 UTC 29 June 1994.

29 June, a large amount of moisture was transported to the location of the SV1 constantly. Consequently, the moisture component of the SV1 was located over regions of (basic-state) high moisture availability from 1300 UTC to 1600 UTC.

Continuous moisture transport between cyclonic circulation (north of the precipitating system) and anticyclonic circulation (south of the precipitating system) created favorable conditions for precipitation (Fig. 10). Potential temperature at the center of the system increased with height, and hence the system was statically stable (Fig. 10b). However, equivalent potential temperature at the center of the system decreased with height from the 0.95-sigma level to the 0.55-sigma level by ∼10 K, and hence the system was conditionally unstable (Fig. 10b). Maximum of column-integrated moisture flux convergence appeared at the center of the system, implying that a large amount of precipitation can be induced by the cumulus parameterization (subgrid-scale) scheme (Fig. 10a). In addition, relative humidity at the center of the system was almost 100%, implying that a large amount of precipitation can be induced by the large-scale condensation (grid-scale) scheme (Fig. 10a). Consequently, high moisture availability at the center of the system resulted in a large amount of both convective and nonconvective precipitation, and this precipitation turned out to be connected to the vertical propagation of the SV1 energy.

Figure 11 shows vertical distributions of the SV1 energy at 1800 UTC 29 June, 2200 UTC 29 June, and 0500 UTC 30 June 1994. At 1800 UTC 29 June, the kinetic energy was comparable to the moisture-component energy at the 0.85-sigma level, and it appeared as another peak at the 0.15-sigma level (∼192 hPa, Fig. 11a). Afterward, two peaks appeared in the vertical profile of the SV1 energy. One major peak was related to the upper-level kinetic energy, and the other minor peak was related to the lower-level kinetic energy or the moisture-component energy. At 2200 UTC 29 June, the kinetic energy was dominant at the 0.25-sigma level, and a minor peak appeared at the 0.85-sigma level (Fig. 11b). This minor peak was composed of the kinetic energy and the moisture-component energy, and the kinetic energy was dominant. At 0500 UTC 30 June, the kinetic energy was dominant at the 0.25-sigma level, and a minor peak appeared at the 0.75-sigma level (Fig. 11c). In contrast with the dominance of the kinetic energy at 2200 UTC 29 June, the moisture-component energy was dominant in the minor peak at 0500 UTC 30 June. From 1800 UTC 29 June to 0300 UTC 30 June, the kinetic energy was dominant in the lower-level minor peak, and the moisture-component energy was dominant in the lower-level minor peak after 0300 UTC 30 June. Except for the dominant type of energy in the minor peak, the kinetic energy at upper levels peaked from 1800 UTC 29 June to 1200 UTC 30 June.

The horizontal distributions of the zonal wind component and the meridional wind component of the SV1

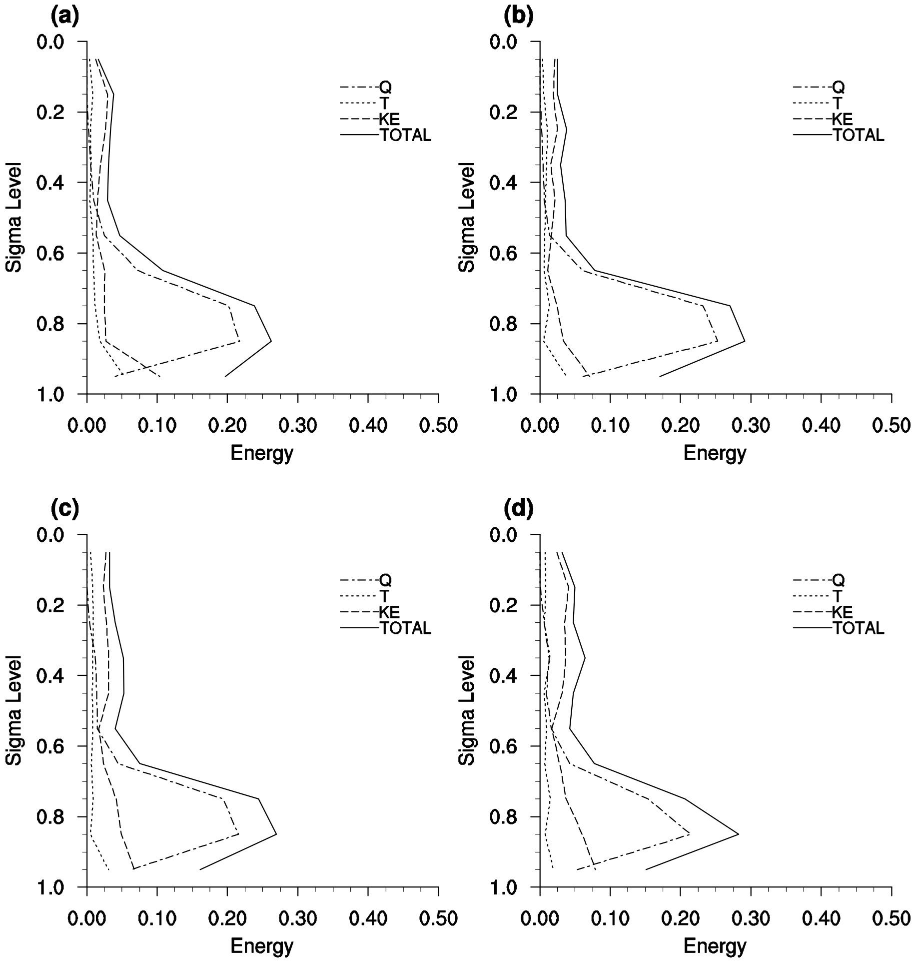

Fig. 8. Vertical profile of SV1 total energy (J kg^{-1}, solid line), kinetic energy (J kg^{-1}, dashed line), temperature-component energy (J kg^{-1}, dotted line), and moisture-component energy (J kg^{-1}, dash-dotted line) computed from nonlinear growth of initial SV1 on 29 June 1994 at (a) 1300 UTC, (b) 1400 UTC, (c) 1500 UTC, and (d) 1600 UTC.

at 1800 UTC 29 June 1994 are shown in Fig. 12. Convergence can be found from the pattern of the zonal wind and meridional wind components of the SV1 at the 0.85-sigma level. In contrast, divergence can be seen from the pattern of the zonal wind and meridional wind components of the SV1 at the 0.15-sigma level. Therefore, the zonal wind and meridional wind components of the SV1 at 1800 UTC 29 June can be summarized as the upper-level divergence and the lower-level convergence. The amplitude of the upper-level divergence was greater than that of the lower-level convergence. Accordingly, the upper-level divergence of the SV1 was possibly responsible for the upper-level kinetic energy peak in the energy profile of the SV1.

Figure 13 shows the 1-h accumulated precipitation and vertical cross sections of latent heating, vertical velocity, and divergence at 2200 UTC 29 June and 0500 UTC 30 June 1994. At 2200 UTC 29 June, the maximum precipitation amount occurred over the Yellow Sea, and nonconvective precipitation was dominant at the maximum (Fig. 13a). Latent heat was released as a result of precipitation, and its maximum appeared at the 0.5-sigma level (~525 hPa). This latent heating enhanced buoyancy, and vertical motion was strongest at the 0.5-sigma level because of the enhanced buoyancy. By the continuity equation (i.e., mass conservation equation), the vertical motion induced convergence at lower levels and divergence at upper levels (Fig. 13b). This lower-level convergence of warm and moist air again resulted in favorable conditions for precipitation, and hence positive feedback existed. At 0500 UTC 30 June, the maximum of precipitation amount occurred over the Korean Peninsula, and convective precipitation was dominant (Fig. 13c). The maximum of latent heating appeared at a relatively high level, the 0.3-sigma level (~335 hPa).

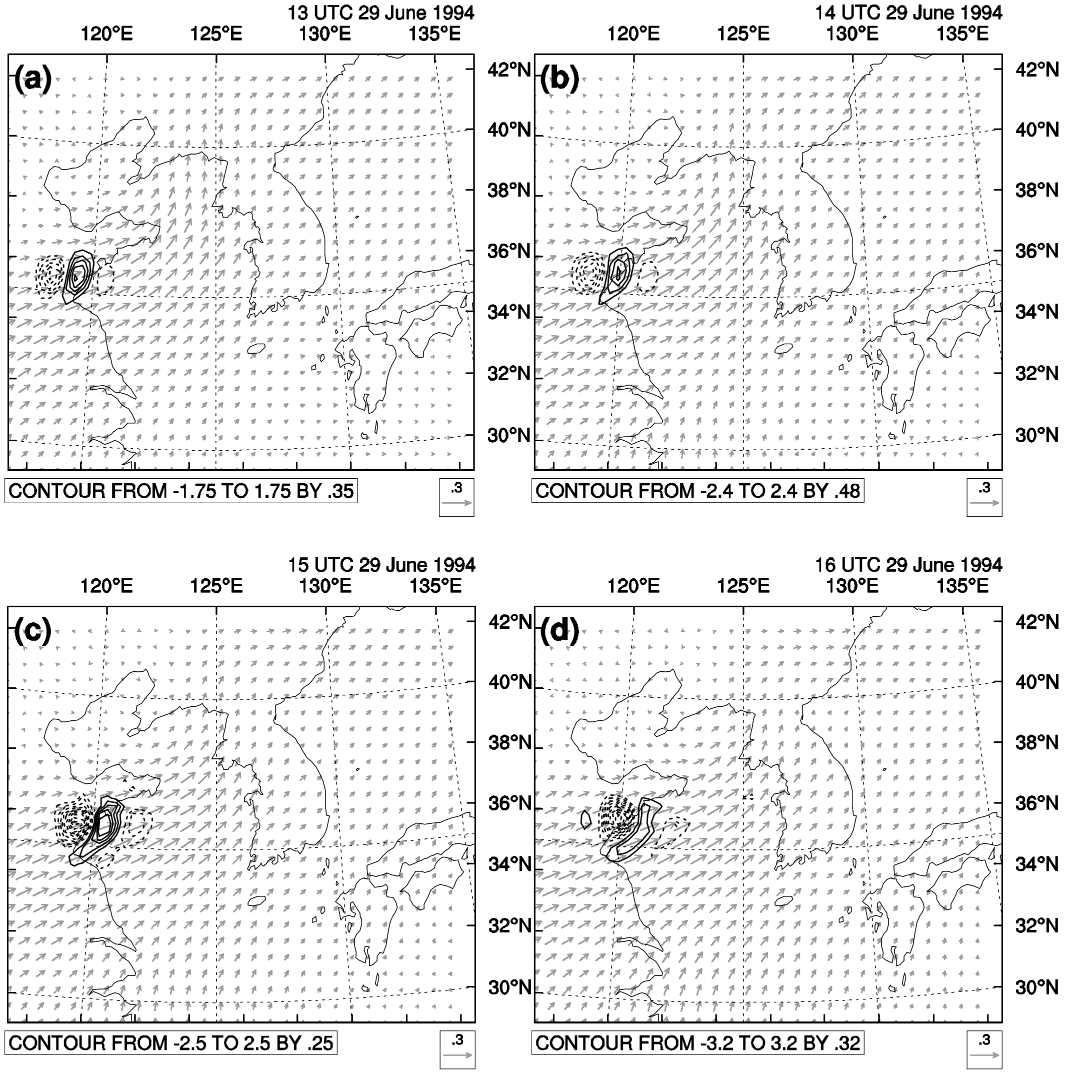

Fig. 9. Moisture component of SV1 computed from nonlinear growth of initial SV1 (g kg^{-1}, negative values are denoted by dashed contours) and moisture flux vector of the basic state (kg m^{-2} s^{-1}) on 29 June 1994 at (a) 1300 UTC, (b) 1400 UTC, (c) 1500 UTC, and (d) 1600 UTC. All quantities were calculated at the 0.85-sigma level.

Vertical motion was strong at upper levels because of the enhanced buoyancy. The corresponding divergence and convergence patterns are shown in Fig. 13d.

In brief, the continuous moisture transport resulted in a large amount of precipitation and the corresponding latent heating. This latent heating enhanced buoyancy, and the enhanced buoyancy induced vertical motion and the corresponding upper-level divergence and lower-level convergence. These features of the basic state were properly reflected in the horizontal distributions of the zonal wind and meridional wind components of the SV1. The vertical propagation of the SV1 energy, from the lower level to the upper level, and the conversion of the SV1 energy, from the moisture-component energy to the kinetic energy, were closely related to precipitation and the corresponding latent heating in the basic state.

The relative ratio between convective and nonconvective precipitation from 1200 UTC 29 June to 1200 UTC 30 June 1994 is shown in Figs. 14a and b with 1-h accumulated precipitation amount averaged over the entire domain. Although the precipitation amount was not large over the entire period because of the spatial average, it increased continuously for the first 9 h and remained nearly constant afterward. Nonconvective precipitation was dominant from 1800 UTC 29 June to 0300 UTC 30 June, and convective precipitation was dominant after 0300 UTC 30 June. This transition from nonconvective precipitation to convective precipitation was also observed in infrared satellite

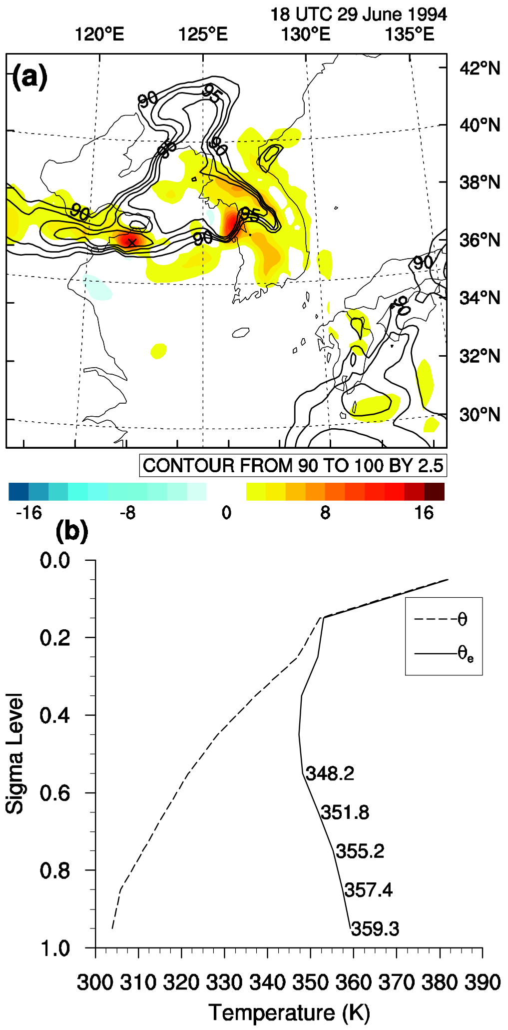

Fig. 10. (a) Horizontal distribution of vertically integrated moisture flux convergence (shaded, 10^{-3} kg m^{-2} s^{-1}) and the 0.85-sigma level relative humidity (contour, >90%) at 1800 UTC 29 June 1994. (b) Vertical structure of potential temperature (K, dashed line) and equivalent potential temperature (K, solid line) calculated at the moisture convergence maximum point denoted by x in (a).

images (Figs. 14c and d). At 1800 UTC 29 June, the horizontal scale of cloud cover was large, and the temperature at the cloud top was relatively high (i.e., cloud-top height was low). In contrast, the horizontal scale of cloud cover was small and the temperature at the cloud top was relatively low (i.e., cloud-top height was high) at 0900 UTC 30 June. The system associated with nonconvective precipitation was characterized by a large horizontal scale and a small vertical scale, and the system associated with convective precipitation had a small horizontal scale and a large vertical scale.

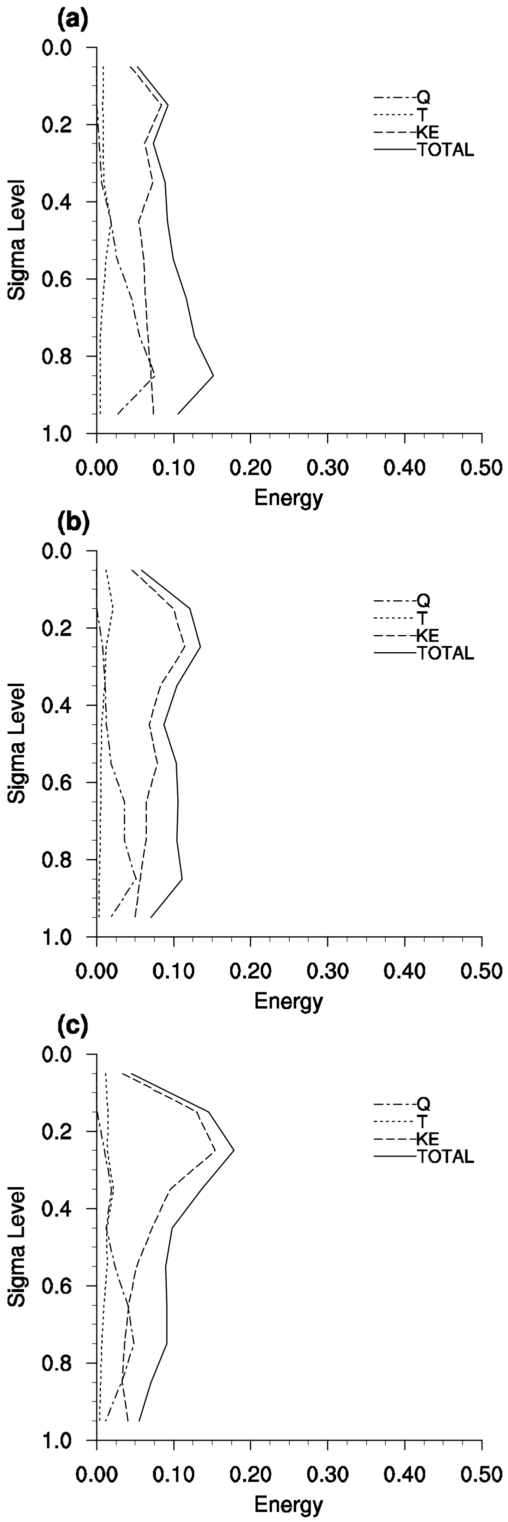

Fig. 11. Same as Fig. 8, but for (a) 1800 UTC 29 June, (b) 2200 UTC 29 June, and (c) 0500 UTC 30 June 1994.

As shown previously in Figs. 11b and c, kinetic energy was dominant from 1800 UTC 29 June to 0300 UTC 30 June, and the moisture-component energy was

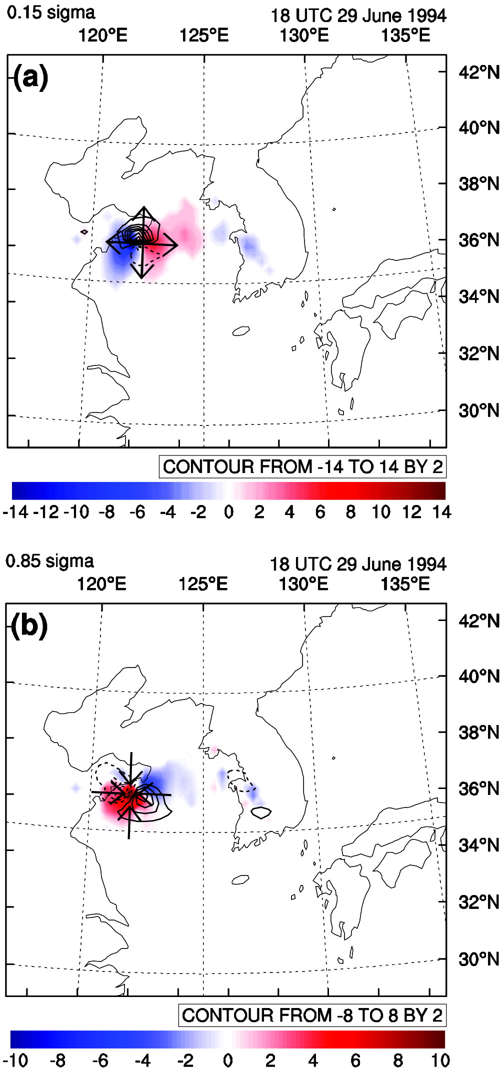

Fig. 12. Zonal wind component (m s^{-1}, shaded) and meridional wind component (m s^{-1}, negative values are denoted by dashed contours) of SV1 at 1800 UTC 29 June 1994 computed from nonlinear growth of initial SV1 for (a) the 0.15-sigma level and (b) the 0.85-sigma level.

dominant after 0300 UTC 30 June in the lower minor peak. This change in the dominant type of the SV1 energy minor peak was related to the transition of the precipitation type in the basic state. From 1800 UTC 29 June to 0300 UTC 30 June, nonconvective precipitation was dominant, and the system associated with the nonconvective precipitation had a relatively small vertical scale. Therefore, the maximum of vertical motion appeared at a lower-middle level, and the corresponding convergence appeared at a relatively low level. The kinetic energy in the lower-level minor peak of the SV1 energy corresponded to the lower-level convergence of the basic state. After 0300 UTC 30 June, convective precipitation was dominant, and the system associated with the convective precipitation had a large vertical scale. The maximum of vertical motion and the corresponding convergence shifted to the mid-upper level, and hence the moisture-component energy related to the moisture transport in the basic state was dominant in the minor peak of the SV1 energy profile.

The temporal variation in the vertical profile of the SV1 energy can be summarized as follows. At the initial time, the temperature-component energy was dominant at the lower level, and this was related to the lower-level baroclinicity of the basic state. After the initial time, the moisture-component energy at the lower levels was dominant for ~4 h. This 4-h dominance of the moisture-component energy was related to the moisture transport in the basic state. From 1800 UTC 29 June to 1200 UTC 30 June 1994, the kinetic energy at the upper levels was prominent in the vertical profile of the SV1 energy. During this period, latent heat resulting from convective and nonconvective precipitation was released, and this latent heating enhanced buoyancy. Vertical motion increased due to the enhanced buoyancy. Finally, divergence appeared above the rising motion and convergence appeared below the rising motion, and this divergence was related to the kinetic energy at the upper levels in the SV1 energy profile. The divergence was greater than the corresponding convergence in the basic state (Figs. 13b and d), and this characteristic of the basic state was reflected in the horizontal distribution (Fig. 12) and the energy profile (Figs. 11b and c) of the SV1. From 1800 UTC 29 June to 0300 UTC 30 June 1994, nonconvective precipitation was dominant. The maximum vertical motion appeared at the middle level, and convergence occurred at the lower levels. This lower-level convergence in the basic state corresponds to the kinetic-energy minor peak at the lower level in the SV1 energy profile. After 0300 UTC 30 June, convective precipitation was dominant. The maximum vertical motion appeared at the upper level, and the convergence occurred at the mid-upper levels. Although the kinetic-energy peak at the upper level in the SV1 energy profile was associated with the upper-level divergence in the basic state, the mid-upper level convergence in the basic state contributed to the kinetic energy at the mid-upper levels in the SV1 energy profile. The moisture-component energy, which was related to the moisture transport in the basic state, was dominant at the lower-level minor peak of the SV1 energy profile. Compared to the period when nonconvective precipitation was dominant, the upper-level divergence in the basic state increased (Figs. 13b and d), and this change in the basic state is reflected in the SV1 energy profile (Fig. 11b and c).

Figure 15 shows vertical distributions of the SV1

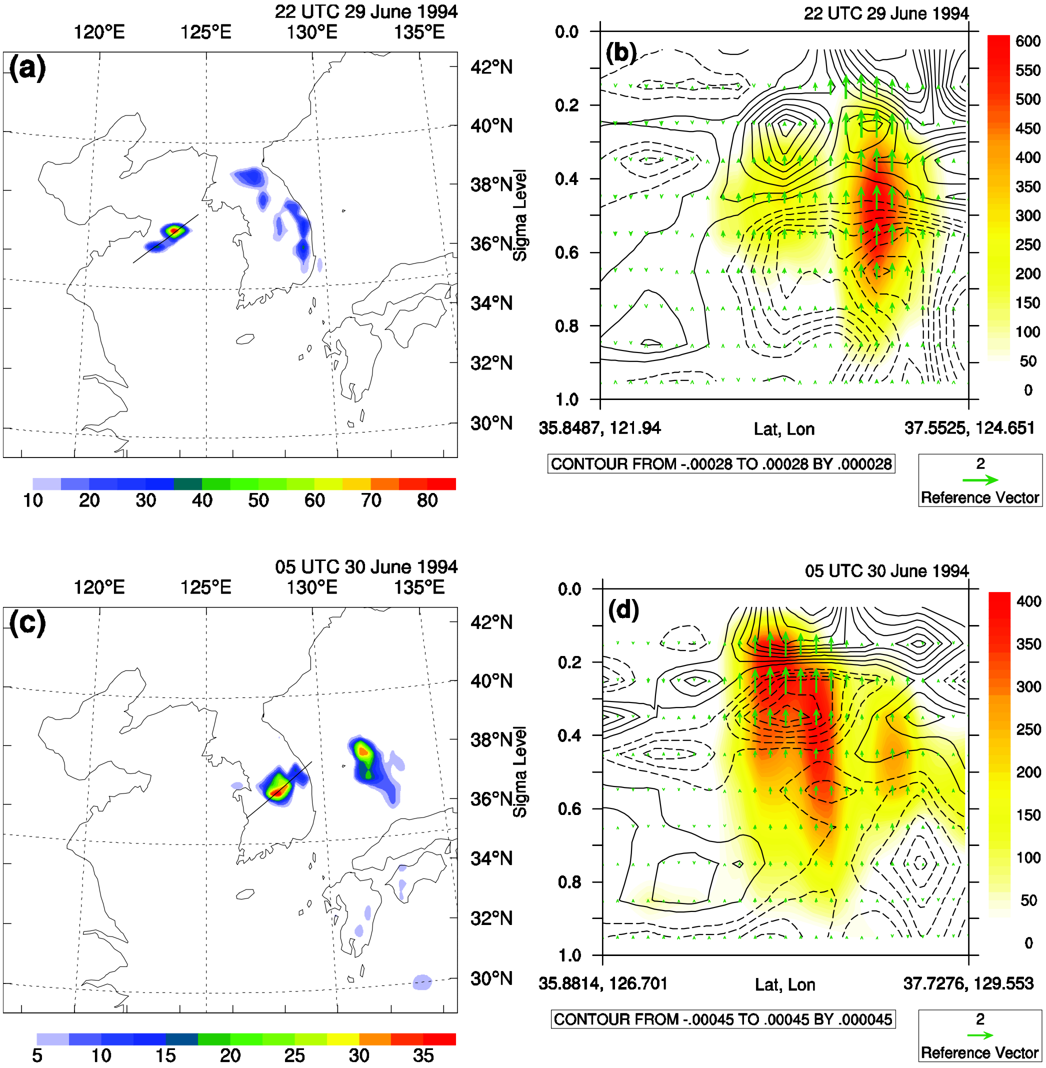

Fig. 13. (a) Horizontal distribution of 1-h accumulated precipitation amount (shaded, mm) at 2200 UTC 29 June 1994. (b) Vertical cross section along the line in (a) of latent heating (shaded, 10^{-5} K s^{-1}), divergence (s^{-1}, negative values are denoted by dashed contours), and vertical-motion vector (m s^{-1}) at 2200 UTC 29 June 1994. (c) Same as (a), but for 0500 UTC 30 June 1994. (d) Same as (b), but for 0500 UTC 30 June 1994.

energy computed from a fake dry experiment. In the fake dry experiment, two experiments, CONTROL and PERTURBED were performed without the latent heating caused by the (nonconvective and convective) precipitation processes. At 1200 UTC 29 June, the temperature-component energy was dominant at the 0.85-sigma level, and the moisture-component energy was dominant at lower levels at 1300 UTC 29 June 1994. These features are equivalent to those of the previous experiment. However, the moisture-component energy was still dominant at the 0.85-sigma level even at 1200 UTC 30 June. This result emphasizes the importance of latent heating caused by the precipitation in the vertical propagation, from the lower level to the upper level, and the transition, from potential energy to kinetic energy, of the SV1 energy.

Additional experiments, where the moisture convergence decreased or increased gradually during the optimization time interval, were conducted to investigate the effect of moisture in the propagation and transition of the SV1 energy. When the moisture convergence decreased, the propagation of the SV1 energy from the lower level to the upper level and the transition of the SV1 energy from the moisture-component energy to the kinetic energy were delayed and weakened. Conversely, when the moisture convergence increased, the propagation of the SV1 energy from the lower level to the upper level and the transition of the

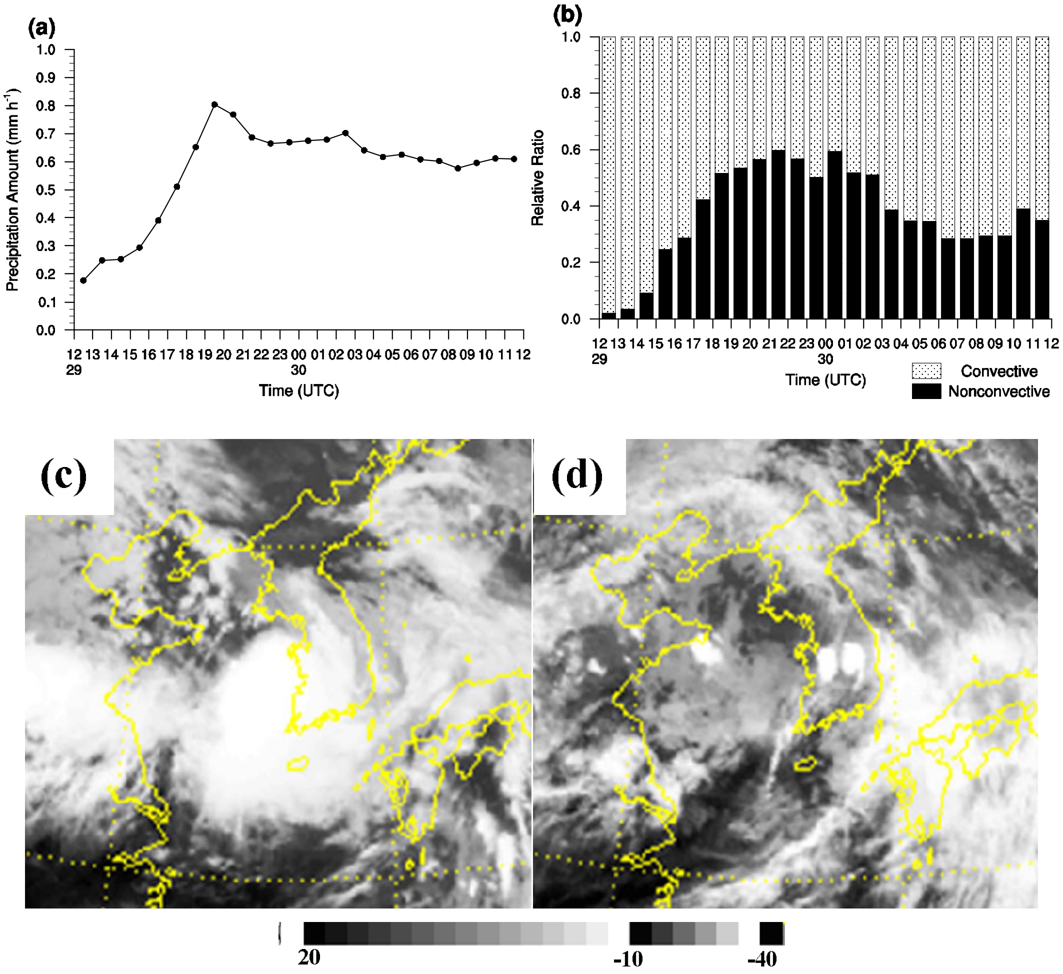

Fig. 14. (a) Time series of domain-averaged 1-h accumulated precipitation (mm). (b) Relative ratio of convective or nonconvective precipitation to total precipitation as a function of time. Satellite infrared image at (c) 1800 UTC 29 June and (d) 0900 UTC on 30 June 1994.

SV1 energy from the moisture–component energy to the kinetic energy were accelerated and strengthened (figures not shown). This implies the importance of moisture in the nonlinear evolution of the SV1 energy.

It is essential to evaluate the linearity assumption on which the singular vector calculation is based, as mentioned in Errico and Raeder (1999). The ratios of the linearly evolved SV1 to the nonlinearly evolved SV1 for the zonal wind, meridional wind, temperature, and moisture components of the SV1 were 1.45, 1.51, 1.41, and 1.22, respectively. The ratios were calculated at the optimization time and in the entire domain. These ratios were used to verify the linearity assumption in Zou et al. (1997), and Kim and Jung (2009a, b). Instead of using infinitesimal amplitude perturbations, the initial SV1 was used as finite-amplitude perturbations for the linearity assumption test in this study. In detail, the initial SV1 was rescaled to have maximum amplitude of typical analysis error (or uncertainty) as suggested by Errico and Raeder (1999). The maximum amplitudes of the initial perturbations were 4 m s^{-1} for the zonal and meridional wind components, 2 K for the temperature component, and 0.001 kg kg^{-1} for the moisture component. Overall, linear growth was greater than nonlinear growth, but the difference between the linear and nonlinear growth was not very large. In spite of this inconsistency in amplitude, the horizontal and vertical structures of the linearly evolved SV1 and nonlinearly evolved SV1 were similar to each other except for minor phase differences (figures not shown).

In summary, the dominance of the temperature-component, moisture-component, and kinetic energy in the SV1 energy profile is closely related to the baroclinic instability (and moisture availability), moisture transport, and upper-level divergence in the basic state, respectively. The nonlinear growth of the SV1 and the temporal evolution of the basic state were ap-

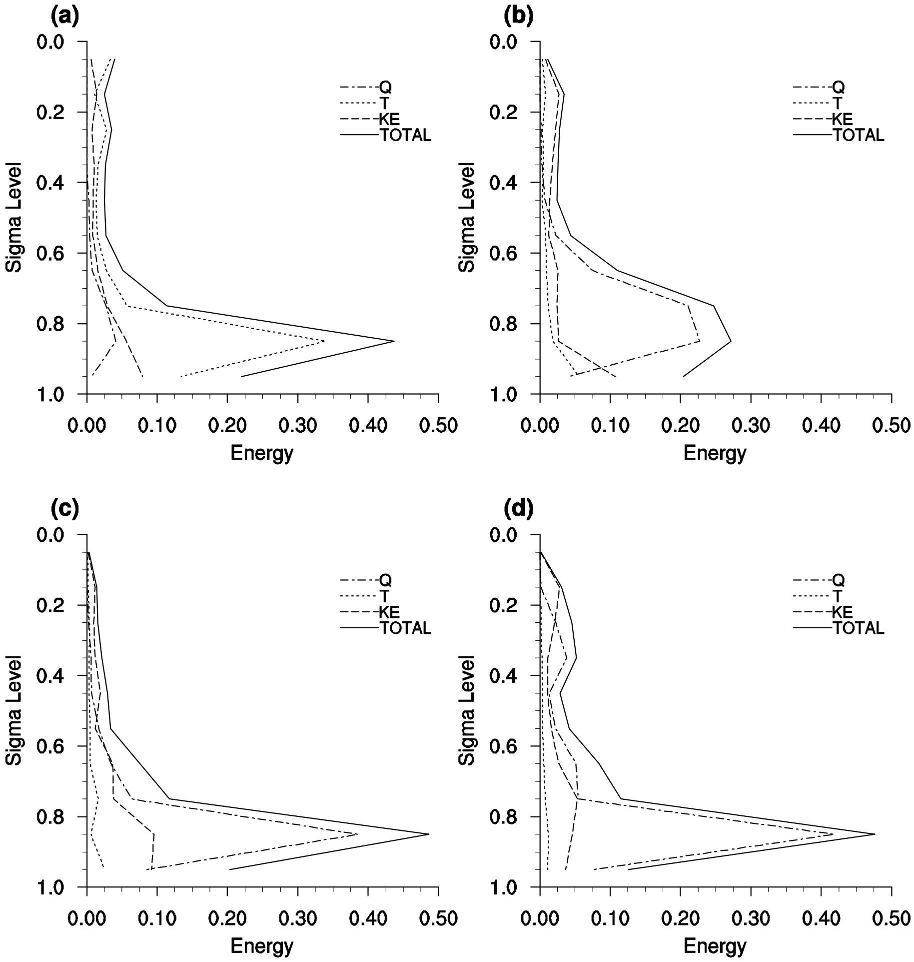

Fig. 15. Vertical profile of SV1 total energy (J kg^{-1}, solid line), kinetic energy (J kg^{-1}, dashed line), temperature-component energy (J kg^{-1}, dotted line), and moisture-component energy (J kg^{-1}, dash-dotted line) computed from nonlinear growth of initial SV1 without latent-heat release (fake dry experiment) at (a) 1200 UTC 29 June, (b) 1300 UTC 29 June, (c) 1800 UTC 29 June, and (d) 1200 UTC 30 June 1994.

propriately correlated. In particular, the importance of moisture in this heavy rainfall case can be deduced from the nonlinear growth of the SV1 energy.

5. Summary and conclusion

Singular vectors related to a heavy rainfall case over the Korean Peninsula were calculated, and the characteristics and nonlinear growth of the singular vector were analyzed using the MM5 adjoint modeling system. Moist physical processes were included in the tangent linear and adjoint models, and the moist basic state and moist total energy norm were used for the singular-vector calculation. The inclusion of moist linear physics and the use of a moist total energy norm were relevant to the singular-vector calculation related to a heavy rainfall case.

The horizontal location of the initial SV1 was near the Shandong Peninsula, and it coincided with the initial location of the surface low. The final SV1 occurred over the East Sea (Sea of Japan), downstream of the initial location. The temperature-component energy at the lower level was converted into kinetic energy at the upper level. This energy conversion from mass fields to wind fields is typical of midlatitude phenomena, and it is consistent with the results of previous studies on extratropical cyclones. Although the upscale energy transfer reported in previous studies was not clearly observed in this study, large-scale energy increased significantly compared to small-scale energy.

In this study, the nonlinear growth of the singular vector was closely related to the basic state. The SV1 occurred over regions of high baroclinicity index, but its exact location shifted to the local maximum of moisture availability at the initial time (1200 UTC 29 June 1994). The temperature-component energy at the lower level was dominant initially, but the moisture-component energy at the lower levels was dominant from 1300 UTC 29 June to 1700 UTC 29 June 1994. This 4-h dominance of the moisture-component energy at lower levels reflects continuous moisture transport in the basic state. The continuous moisture transport constructs favorable conditions for both convective and nonconvective precipitation. There were two peaks in the vertical profile of the singular vector energy from 1800 UTC 29 June to 1200 UTC 30 June 1994 (the final time). One major peak was related to the kinetic energy at upper levels and the other minor peak was related to the kinetic energy (from 1800 UTC 29 June to 0300 UTC 30 June) or the moisture-component energy (from 0400 UTC 30 June to 1200 UTC 30 June) at lower levels. After 1800 UTC 29 June, a large amount of precipitation occurred, and the corresponding latent heat was released. This latent heating induced strong vertical motion, and then divergence appeared at upper levels and convergence appeared at lower levels. The vertical propagation of the singular-vector energy from the lower level to the upper level and the conversion from the moisture-component energy to kinetic energy reflect the upper-level divergence caused by precipitation in the basic state. From 1800 UTC 29 June to 0300 UTC 30 June, nonconvective precipitation was dominant, and convective precipitation was dominant after 0300 UTC 30 June. This change in the dominant type of precipitation was reflected in the variation of the minor peak.

The singular vector for the heavy rainfall case examined in this study showed more localized structures and a larger growth rate than did the singular vectors for extratropical or tropical cases in previous studies. In previous studies, unshielding and untilting have been suggested as growth mechanisms of the singular vector calculated from dry global adjoint systems. In this study, we revealed that latent heating due to precipitation was responsible for the nonlinear growth of the singular vector calculated from moist version of the MM5 adjoint modeling system. The crucial role of the latent heating in the singular-vector growth and the dominance of the moisture-component energy at relatively earlier times emphasize the importance of moisture availability in heavy rainfall cases over the Korean Peninsula.

In this study, our conclusion has been drawn from a particular case, and hence cannot be generalized. To generalize the findings of this study, it will be necessary to analyze singular vectors from a variety of cases. However, the results from this study do support applications of singular vectors to target (or adaptive) observations and ensemble forecasting in spite of the linearity restriction.

Acknowledgements. The authors thank two anonymous reviewers for their valuable comments. This work was funded by the Korea Meteorological Administration Research and Development Program (Grant No. RACS_2010-2016). This research was also supported by Leading Foreign Research Institute Recruitment Program through the National Research Foundation of Korea (NRF) funded by the Ministry of Education, Science and Technology (MEST) (2010-00715) and by the Brain Korea 21 Project. The authors are grateful for computing resources provided by the Korea Institute of Science and Technology Information under "The Strategic Supercomputing Support Program" .

REFERENCES

Badger, J., and B. J. Hoskins, 2001: Simple initial value problems and mechanisms for baroclinic growth. *J. Atmos. Sci.*, **58**, 38–49.

Buizza, R., and T. N. Palmer, 1995: The singular-vector structure of the atmospheric global circulation. *J. Atmos. Sci.*, **52**, 1434–1456.

Buizza, R., and A. Montani, 1999: Targeting observations using singular vectors. *J. Atmos. Sci.*, **56**, 2965–2985.

Buizza, R., J. Tribbia, F. Molteni, and T. N. Palmer, 1993: Computation of optimal unstable structures for a numerical weather prediction model. *Tellus*, **45**, 388–407.

Coutinho, M. M., B. J. Hoskins, and R. Buizza, 2004: The influence of physical processes on extratropical singular vectors. *J. Atmos. Sci.*, **61**, 195–209.

Denis, B., J. Cote, and R. Laprise, 2002: Spectral decomposition of two-dimensional atmospheric fields on limited-area domains using the Discrete Cosine Transform (DCT). *Mon. Wea. Rev.*, **130**, 1812–1829.

Ehrendorfer, M., and R. M. Errico, 1995: Mesoscale predictability and optimal perturbations. *J. Atmos. Sci.*, **52**, 3475–3500.

Ehrendorfer, M., and J. J. Tribbia, 1997: Optimal prediction of forecast error covariances through singular vectors. *J. Atmos. Sci.*, **54**, 3475–3500.

Ehrendorfer, M., R. M. Errico, and K. D. Raeder, 1999: Singular-vector perturbation growth in a primitive equation model with moist physics. *J. Atmos. Sci.*, **56**, 1627–1648.

Errico, R. M., and K. D. Raeder, 1999: An examination of the accuracy of the linearization of a mesoscale model with moist physics. *Quart. J. Roy. Meteor. Soc.*, **125**, 169–195.

Errico, R. M., K. Raeder, and T. Vukicevic, 1994: Mesoscale Adjoint Modeling System version 1 (MAMS1). NCAR Tech. Note NCAR/TN-410+1A, 214pp.

Errico, R. M., M. Ehrendorfer, and K. D. Raeder, 2001: The spectra of singular values in a regional model. *Tellus*, **53**, 317–332.

Errico, R. M., K. Raeder, and M. Ehrendorfer, 2004: Singular vectors for moisture-measuring norms. *Quart. J. Roy. Meteor. Soc.*, **130**, 963–987.

Farrell, B. F., 1990: Small error dynamics and the predictability of atmospheric flows. *J. Atmos. Sci.*, **47**, 2409–2416.

Gelaro, R., R. Buizza, T. N. Palmer, and E. Klinker, 1998: Sensitivity analysis of forecast errors and the construction of optimal perturbations using singular vectors. *J. Atmos. Sci.*, **55**, 1012–1037.

Gelaro, R., R. H. Langland, G. D. Rohaly, and T. E. Rosmond, 1999: An assessment of the singular-vector approach to targeted observing using the FASTEX data set. *Quart. J. Roy. Meteor. Soc.*, **125**, 3299–3327.

Grell, G. A., J. Dudhia, and D. R. Stauffer, 1993: A description of the fifth generation Penn State/NCAR me- soscale model (MM5). NCAR Tech. Note NCAR/TN-398+STR, 117pp.

Hamill, T. M., C. Snyder, and R. E. Morss, 2000: A comparison of probabilistic forecasts from bred, singular-vector, and perturbed observation ensembles. *Mon. Wea. Rev.*, **128**, 1835–1851.

Hoskins, B. J., and P. J. Valdes, 1990: On the existence of storm-tracks. *J. Atmos. Sci.*, **47**, 1855–1864.

Hoskins, B. J., and M. M. Coutinho, 2005: Moist singular vectors and the predictability of some high impact European cyclones. *Quart. J. Roy. Meteor. Soc.*, **131**, 581–601.

Hoskins, B. J., R. Buizza, and J. Badger, 2000: The nature of singular vector growth and structure. *Quart. J. Roy. Meteor. Soc.*, **126**, 1565–1580.

Kalnay, E., 2004: *Atmospheric Modeling, Data Assimilation and Predictability.* Cambridge, 341pp.

Kim, H. M., and M. C. Morgan, 2002: Dependence of singular vector structure and evolution on the choice of norm. *J. Atmos. Sci.*, **59**, 3099–3116.

Kim, H. M., and B.-J. Jung, 2009a: Singular vector structure and evolution of a recurving tropical cyclone. *Mon. Wea. Rev.*, **137**, 505–524.

Kim, H. M., and B.-J. Jung, 2009b: Influence of moist physics and norms on singular vectors for a tropical cyclone. *Mon. Wea. Rev.*, **137**, 525–543.

Kuo, H. L., 1974: Further studies of the parameterization of the influence of cumulus convection on large scale flow. *J. Atmos. Sci.*, **31**, 1232–1240.

Lee, D.-K., J.-G. Park, and J.-W. Kim, 2008: Heavy rainfall events lasting 18 days from July 31 to August 17, 1998, over Korea. *J. Meteor. Soc. Japan*, **86**, 313–333.

Lorenz, E. N., 1965: A study of the predictability of a 28-variable atmospheric model. *Tellus*, **17**, 321–333.

Majumdar, S. J., C. H. Bishop, R. Buizza, and R. Gelaro, 2002: A comparison of ensemble-transform Kalman-filter targeting guidance with ECMWF and NRL total-energy singular-vector guidance. *Quart. J. Roy. Meteor. Soc.*, **128**, 2527–2549.

Majumdar, S. J., S. D. Aberson, C. H. Bishop, R. Buizza, M. S. Peng, and C. A. Reynolds, 2006: A comparison of adaptive observing guidance for Atlantic tropical cyclones. *Mon. Wea. Rev.*, **134**, 2354–2372.

Molteni, F., R. Buizza, T. N. Palmer, and T. Petroliagis, 1996: The ECMWF ensemble prediction system: Methodology and validation. *Quart. J. Roy. Meteor. Soc.*, **122**, 73–119.

Montani, A., and A. J. Thorpe, 2002: Mechanism leading to singular-vector growth for FASTEX cyclones. *Quart. J. Roy. Meteor. Soc.*, **128**, 131–148.

NAG, 2005: NAG Fortran Library Manual Mark 21.

Palmer, T. N., 1996: Predictability of the atmosphere and oceans: From days to decades. *Decadal Climate Variability-Dynamics and Predictability*, Anderson and Willebrand, Eds., NATO ASI Series, Subseries Ⅰ, *Global Environmental Change*, Vol. 44, Springer, 83–155.

Reynolds, C. A., R. Gelaro, and J. D. Doyle, 2001: Relationship between singular vectors and transient features in the background flow. *Quart. J. Roy. Meteor. Soc.*, **127**, 1731–1760.

Strang, G., 1986: *Introduction to Applied Mathematics.* Wellesley-Cambridge Press, 758pp.

Vukicevic, T., and R. M. Errico, 1993: Linearization and adjoint of parameterized moist diabatic processes. *Tellus*, **45**, 493–510.

Wu, C.-C., and Coauthors, 2009: Intercomparison of targeted observation guidance for tropical cyclones in the northwestern Pacific. *Mon. Wea. Rev.*, **137**, 2471–2492.

Yamaguchi, M., T. Iriguchi, T. Nakazawa, and C.-C. Wu, 2009: An observing system experiment for Typhoon Conson (2004) using a singular vector method and DOTSTAR data. *Mon. Wea. Rev.*, **137**, 2801–2816.

Zou, X., W. Huang, and Q. Xiao, 1998: A user's guide to the MM5 adjoint modeling system. NCAR Tech. Note NCAR/TN-435TR, 94pp.

Zou, X., F. Vandenberghe, M. Pondeca, and Y.-H. Kuo, 1997: Introduction to adjoint techniques and the MM5 adjoint modeling system. NCAR Tech. Note NCAR/TN-435STR, 110pp.

Zou, X., K. Sriskandarajah, W. Yu, and S.-Q. Zhang, 2001: Eliminating finite-amplitude non-physical oscillations in the time evolution of adjoint model solutions introduced by the leapfrog time-integration scheme. *Tellus*, **53**, 578–584.